The Astrophysical Journal Letters, 909:L5 (9pp), 2021 March 1 https://doi.org/10.3847/2041-8213/abe708

PIC Simulation of Double Plasma Resonance and Zebra Pattern of Solar Radio Bursts

Chuanyang Li[1,2], Yao Chen[1,2], Sulan Ni[1,2], Baolin Tan[3], Hao Ning[1,2], and Zilong Zhang[1,2]
[1] Center for Integrated Research on Space Science, Astronomy, and Physics, Institute of Frontier and Interdisciplinary Science, Shandong University, Qingdao, Shandong, 266237, People's Republic of China; yaochen@sdu.edu.cn
[2] Institute of Space Sciences, Shandong University, Weihai, Shandong 264209, People's Republic of China
[3] Key Laboratory of Solar Activity, National Astronomical Observatories of Chinese Academy of Sciences, Beijing, People's Republic of China
Received 2020 December 17; revised 2021 February 8; accepted 2021 February 16; published 2021 March 2

Abstract

The latest study has reported that plasma emission can be generated by energetic electrons of Dory–Guest–Harris distribution via the electron cyclotron maser instability (ECMI) in plasmas characterized by a large ratio of plasma oscillation frequency to electron gyro-frequency (ω_{pe}/Ω_{ce}). In our study, on the basis of the ECMI-plasma emission mechanism, we examine the double plasma resonance (DPR) effect and the corresponding plasma emission at both harmonic (H) and fundamental (F) bands using particle-in-cell simulations with various ω_{pe}/Ω_{ce}. This allows us to directly simulate the feature of the zebra pattern (ZP) observed in solar radio bursts for the first time. We find that (1) the simulations reproduce the DPR effect nicely for the upper hybrid and Z modes, as seen from their variation of intensity and linear growth rate with ω_{pe}/Ω_{ce}, (2) the intensity of the H emission is stronger than that of the F emission by ~2 orders of magnitude and varies periodically with increasing ω_{pe}/Ω_{ce}, while the F emission is too weak to be significant (therefore, we suggest that it is the H emission accounting for solar ZPs), (3) the peak-valley contrast of the total intensity of H is ~4, and the peak lies around integer values of ω_{pe}/Ω_{ce} (=10 and 11) for the present parameter setup. We also evaluate the effect of energy of energetic electrons on the characteristics of ECMI-excited waves and plasma radiation. The study provides novel insight on the physical origin of ZPs of solar radio bursts.

Unified Astronomy Thesaurus concepts: Plasma astrophysics (1261); Radio bursts (1339); Solar corona (1483); Solar activity (1475); Solar coronal radio emission (1993)

1. Introduction

Zebra patterns (ZPs) represent a kind of spectral fine structure with equidistant or almost-equidistant stripes of enhanced intensity against a broadband background, frequently observed in dynamic spectra of solar radio bursts such as type IVs (Slottje 1972; Chernov et al. 2012). ZPs receive a lot of attention not only because of their intriguing and perplexing manifestation, but also because of their scientific values in diagnosing coronal parameters such as magnetic field strength within the source of radio bursts. Many models of ZPs have been proposed (Kuijpers 1975a, 1975b; Zheleznyakov & Zlotnik 1975; Chernov 1990; LaBelle et al. 2003; Kuznetsov 2005; Ledenev et al. 2006; Tan 2010; Karlický 2013; see Chernov 2011 and Tan et al. 2014a for a review). Among them, the well-accepted one is the so-called double plasma resonance (DPR) model. The effect of DPR is associated with plasma kinetic instability excited by energetic electrons in the parameter regime of $\omega_{pe}/\Omega_{ce} \gg 1$, where ω_{pe}/Ω_{ce} is the ratio of plasma frequency ω_{pe} to electron gyro-frequency Ω_{ce}. It results in sharply increased growth rates of plasma waves such as the upper hybrid (UH) mode when the UH frequency ($\omega_{\rm UH} = \sqrt{\omega_{pe}^2 + \Omega_{ce}^2}$) is equal to s times of Ω_{ce} ($\omega_{\rm UH} \approx s\Omega_{ce}$), where s is an integer (Zheleznyakov & Zlotnik 1975; Zlotnik 2013, see Zheleznyakov et al. 2016 for a latest review on DPR).

Previous studies on DPR are mostly linear or quasi-linear analyses of growth rates of electrostatic UH modes (see the two latest studies by Benáček et al. 2017 and Li et al. 2019), which are, however, nonescaping and cannot directly account for bursts of the radio emission. Most studies simply presume that the UH modes can somehow convert to the escaping radiation through the nonlinear mode-coupling process in terms of plasma emission (Winglee & Dulk 1986; Yasnov & Karlický 2004; Benáček et al. 2017). To understand the underlying radiation process, it is necessary to employ a fully kinetic electromagnetic particle-in-cell (PIC) simulation. Yet only a few such studies exist, and they are still limited to investigation of the electrostatic modes. One latest example is the work done by Benáček & Karlický (2019), who studied the effect of ω_{pe}/Ω_{ce} on the growth rate of electrostatic UH waves.

It is generally believed that solar radio continuum bursts like type-IVs are associated with energetic electrons trapped within magnetic structures in the corona (or in the solar wind for interplanetary type-IVs, Smerd & Dulk 1971; Wild & Smerd 1972; Vlahos et al. 1982; Stewart 1985; Benz 2002; see Vasanth et al. 2016, 2019 for lastest observational studies). Most, if not all, earlier theoretical studies on type-IVs employ loss-cone type distributions, such as the classical loss-cone distribution or the Dory–Guest–Harris distribution (DGH; Dory et al. 1965; Winglee & Dulk 1986; Yasnov & Karlický 2004; Benáček et al. 2017; Benáček & Karlický 2018; Li et al. 2019). Using the DGH distribution, Ni et al. (2020) investigated the plasma emission process driven by energetic electrons via the electron cyclotron maser instability (ECMI) within a parameter regime of $\omega_{pe}/\Omega_{ce} \gg 1$, while most PIC studies on the ECMI are conducted in the opposite parameter regime ($\omega_{pe}/\Omega_{ce} \ll 1$) within which the well-known electron-cyclotron-maser emission applies (Wu & Lee 1979). The ECMI-plasma emission process starts from linear excitation of waves (like the UH, Z, and whistler (W) modes) by hot DGH electrons within an appropriate coronal background with $\omega_{pe}/\Omega_{ce} \gg 1$, the plasma radiation is suggested to be a result of nonlinear wave–wave coupling or coalescence with the F emission generated through the coupling of almost-counter-propagating Z and W modes,

and H through the coupling of almost-counter-propagating electrostatic UH modes. Resonance conditions can be satisfied as demonstrated by Ni et al. (2020). This radiation process still belongs to the general classification of plasma emission, but is distinct from the traditional beam-driven process (Ginzburg & Zhelezniakov 1958).

This study has two major purposes. One is to further verify the ECMI-plasma emission process proposed by Ni et al. (2020) through detailed parameter study. Ni et al. (2020) only considers one specific parameter with $\omega_{pe}/\Omega_{ce} = 10$, here we present PIC simulations with ω_{pe}/Ω_{ce} varying within two representative gyroharmonic bands (9.5–11.5) so as to simulate the DPR effect. The DPR effect will yield high and low values of growth rates of modes that are excited linearly, thus relevant radiation shall carry the imprint of these variations if the proposed radiation mechanism indeed works. The other purpose is to simulate the development of the DPR effect from linear excitation of nonescaping wave modes to the release of the escaping fundamental (F) and harmonic (H) plasma radiations. This is one necessary step toward a better understanding of ZPs of solar radio bursts such as type-IVs, and done for the first time to our knowledge. The following section introduces the PIC code and the parameter setup. In Section 3 results of the parameter study are presented, followed by the summary and discussion.

2. The PIC Code and Parameter Setup of Simulations

The numerical simulation is performed using the Vector-PIC (VPIC) code developed and released by Los Alamos National Labs. VPIC employs a second-order, explicit, leapfrog algorithm to update charged particle positions and velocities in order to solve the relativistic kinetic equation for each species, along with a full Maxwell description for electric and magnetic fields evolved via a second-order finite-difference time-domain solver (Bowers et al. 2008a, 2008b, 2009).

The background magnetic field is set to be $\boldsymbol{B}_0$ ($=B_0\hat{e}_z$), and the wavevector $\boldsymbol{k}$ is in the xOz plane, so E_y represents the pure transverse component of the wave electric field. Periodic boundary conditions are used. The plasmas consist of three components, including background electrons and protons with an Maxwellian distribution, and energetic electrons with the DGH distribution ($j = 1$) expressed as follows:

$$f_0 = \frac{1}{(2\pi)^{3/2} v_0^3} \exp\left(-\frac{u^2}{2v_0^2}\right),$$
$$f_e = \frac{u_\perp^{2j}}{2^j (2\pi)^{3/2} v_e^{3+2j} j!} \exp\left(-\frac{u_\perp^2 + u_\parallel^2}{2v_e^2}\right), \quad (1)$$

where u_x, u_y, and u_z are momentum per mass of particles, $v_0 = \sqrt{k_B T_0/m_e}$ is the thermal velocity of background electrons with a fixed value of $v_0 = 0.018c$ ($T_0 \sim 2$ MK), and v_e is the mean velocity of energetic electrons. The initial plasma temperature of protons is set to be equal to that of background electrons. The value of v_e will be adjusted as presented in the following section. All particles distribute homogeneously in space.

The simulation domain is set to be $L_x = L_z = 1024\,dx = 1024\,dz$, where $dx = dz = 3.25\,\lambda_D$ is the grid spacing (or cell size), and λ_D is the Debye length of the background electrons. The unit of time is the plasma response time (ω_{pe}^{-1}). The wavenumber range that can be resolved is $[-536, 536]\ \Omega_{ce}/c$, and the resolvable frequency range is $[0, 32]\ \Omega_{ce}$. The resolution in wavenumber is $\sim 1.04\,\Omega_{ce}/c$, and the resolution in frequency is $\sim 0.06\,\Omega_{ce}$ (for the time interval of $1000\ \omega_{pe}^{-1}$). The simulation time is $3500\ \omega_{pe}^{-1}$. The time step dt is $0.7\ dx/(\sqrt{2}c) \sim 0.03\ \omega_{pe}^{-1}$, in accordance with the Courant condition. The NPPC (number of macro-particles for each species in each cell) is taken to be 2000 for the study on the effect of v_e (Section 3.1), and 1000 for the larger set of parameter study on the effect of ω_{pe}/Ω_{ce} to reduce the computational cost (Sections 3.2 and 3.3). Charge neutrality is maintained initially. The proton-to-electron mass ratio of 1836 is used, and the number density ratio of DGH to total electrons is assumed to be 0.1.

3. Numerical Results

According to the latest theoretical analysis of ECMI by Li et al. (2019), the peak-bottom contrast of growth rate for UH or Z mode is in general larger for smaller v_e, thus to reveal as-large-as-possible contrast of wave excitation within the chosen harmonic bands, we set $v_e = 0.15c$. This corresponds to the lowest value investigated by Li et al. (2019). To compare with the already-published results for $v_e = 0.3c$ (Ni et al. 2020), we start from a parameter study on v_e while keeping other parameters and configurations the same as those used in Ni et al. (2020). Two values of v_e, $0.15c$ and $0.4c$, are employed. This gives us three cases for comparison, allowing us to evaluate the effect of v_e on the wave growth and emission properties.

3.1. Effect of v_e on Wave Growth and Emission Properties

Figure 1 shows maps of the maximum wave intensity in the $\boldsymbol{k}$ ($k_\parallel$, $k_\perp$) space during the last stage of simulation ([2500, 3500] ω_{pe}^{-1}), and Figure 2 shows the ω–k dispersion diagram along three different directions. The wave modes exhibited in both figures can be identified with the dispersion curves of the four magneto-ionic modes (X, O, Z, and W) that are superposed onto Figure 2. It should be noted that the O-F mode is quasi-electrostatic here since its frequency is very close to the plasma oscillation frequency, thus the magnetic field energy is much weaker than the electric field energy. In addition, the UH mode is electrostatic, while the Z mode contains both electrostatic and electromagnetic parts. Since the transverse electromagnetic component can be represented by E_y, in this study we use dispersion diagrams of components of the electric field to represent various wave modes.

The large regime with enhanced intensity at large k in Figure 1 belongs to the UH mode (i.e., obliquely propagating Langmuir wave), which is the extension of the Z mode toward large k. Note that a spectral gap exists between the electrostatic UH and the electromagnetic Z mode (see Figure 2). For $v_e = 0.15c$ the gap is in the range of $20\,\Omega_{ce}/c < |k| < 50\,\Omega_{ce}/c$, and for $v_e = 0.4c$ the gap is within $10\,\Omega_{ce}/c < |k| < 20\,\Omega_{ce}/c$. The circular pattern shown in Figure 1 belongs to the H emission, inside the circle are W and Z modes with smaller k. In addition, the W mode is mainly along the quasi-parallel to parallel direction and Z mode mainly along the oblique to perpendicular direction. The O-mode F emission is too weak to be recognized from Figure 1.

Figure 3 presents energy profiles of these modes, which are calculated by integrating energy of the six components of the

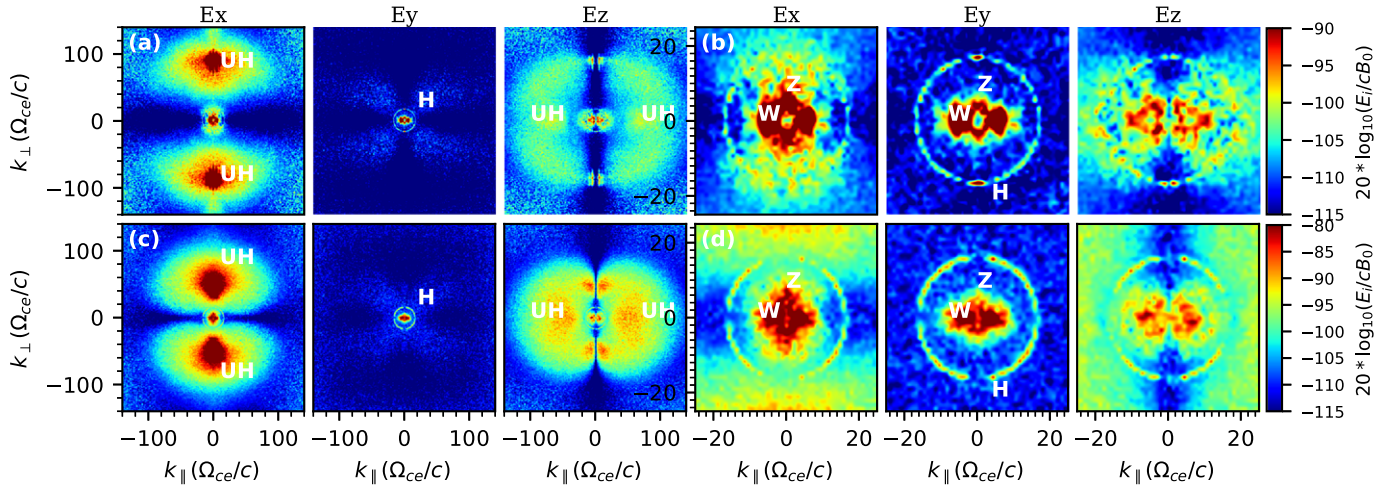

Figure 1. Maximum intensity of (E_x, E_y, E_z) in the ω domain as a function of $k_\parallel$ and $k_\perp$ over the interval of $2500 < \omega_{pe}t < 3500$, as shown by the colormap of $20\log_{10}[(E_x, E_y, E_z)/(cB_0)]$, (a)–(b) for $v_e = 0.15c$ and (c)–(d) for $v_e = 0.4c$. Panels (b) and (d) are zoom-in versions of panels (a) and (c). "UH" stands for upper hybrid mode, "W" for whistler mode, "Z" for Z mode, and "H" for harmonic plasma emission.

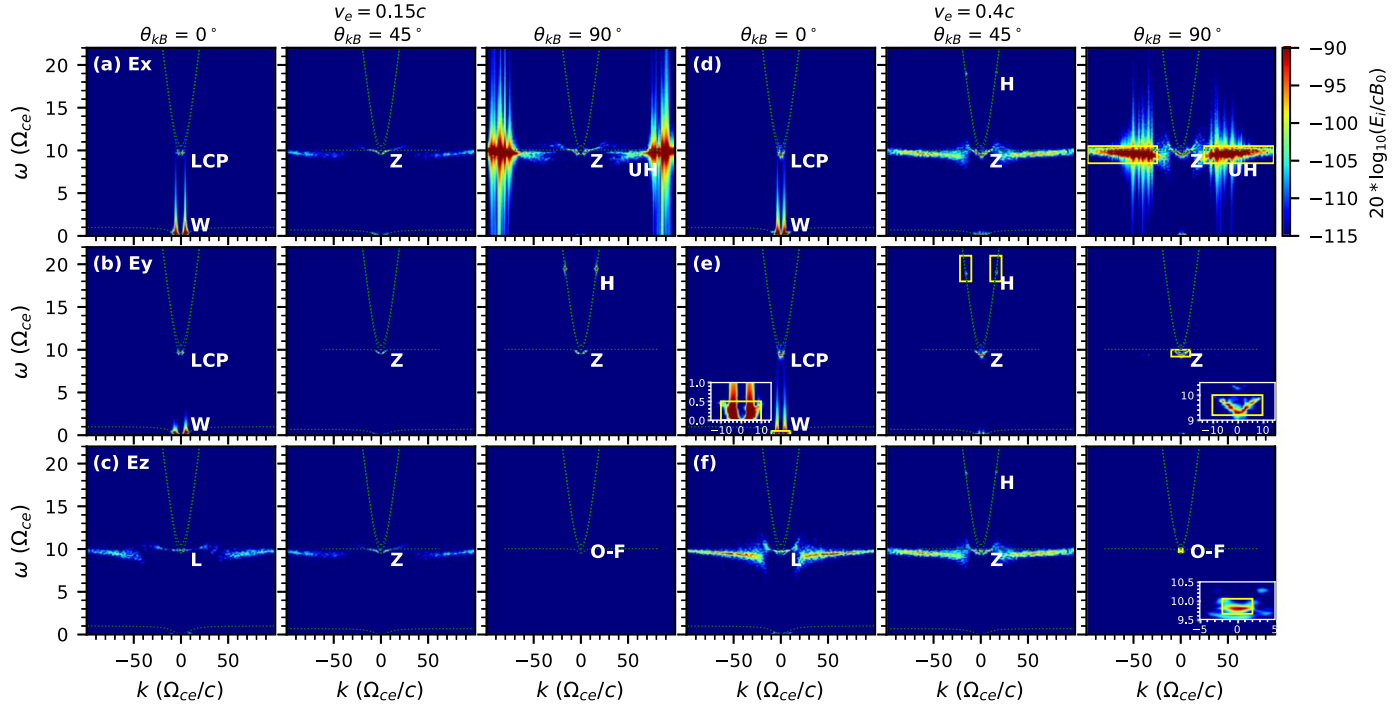

Figure 2. Wave dispersion diagrams of E_x, E_y, and E_z over times $2500 < \omega_{pe}t < 3500$ along directions of 0°, 45°, and 90° (the angle between wavevector and background magnetic field). Left panels (a)–(c) for $v_e = 0.15c$ and right panels (d)–(f) for $v_e = 0.4c$. "L" stands for Langmuir mode, "LCP" for left-circularly polarized wave and "O-F" for O mode around the fundamental plasma frequency. The green dotted lines represent the dispersion curves of four modes (X, O, Z, and W) of the theoretical magneto-ionic theory. The yellow boxes mark the spectral region to calculate the intensity of different wave modes.

electromagnetic field within a respective range of the dispersion curve as indicated by spectral boxes overplotted in Figure 2, according to Parseval's theorem. The UH, W, and H modes are well separated from each other in either frequency or wavenumber. Yet it is difficult to separate the O-F mode from the Z mode along parallel and quasi-parallel propagating directions along which the two modes are somehow connected. We have therefore excluded this part ($\theta_{kB} < 15°$) when calculating the energy of the O-F mode. Note that the thermal noise, even organized along the dispersion curves, presents a minor contribution to the total energy of the excited wave modes (see more details in the Appendix).

As seen from Figure 3, there exist three major consequences as v_e increases from $0.15c$ to $0.4c$.

First is the change of the angular distribution of the UH mode in the $\boldsymbol{k}$ space. For $v_e = 0.15c$, the strongest part of UH grows mainly along the quasi-perpendicular to perpendicular direction within a quite-limited range of propagation angles (~82°–98°), the range of k is also quite limited (~60–100 Ω_{ce}/c), both ranges are much smaller than their counterparts for larger v_e. For other modes, such as Z and W, the distribution patterns do not change obviously with increasing v_e, except the intensities become stronger and the Z mode extends to smaller k (~0). Values of k of UH get smaller for larger v_e, so as to meet the condition of the wave-

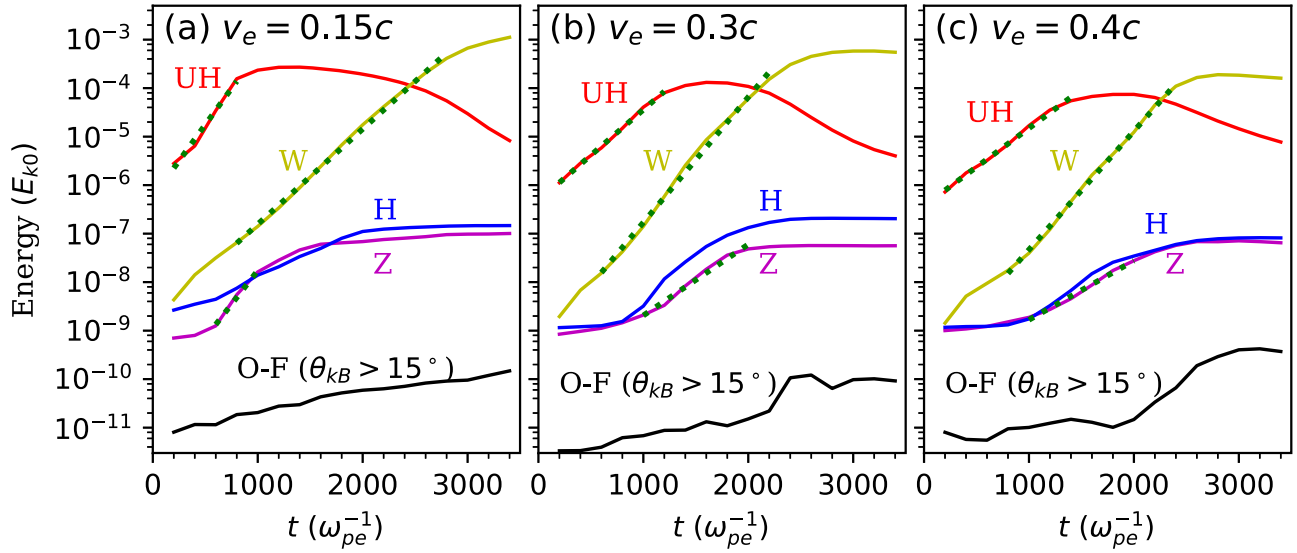

Figure 3. The temporal energy profiles of UH, Z, W, H, and O-F modes with $\omega_{pe}/\Omega_{ce} = 10$ and (a) $v_e = 0.15c$, (b) $v_e = 0.3c$, and (c) $v_e = 0.4c$, normalized to the respective initial kinetic energy of total electrons (E_{k0}). Among them, the energy of the O-F mode is integrated in the range of $\theta_{kB} > 15°$ to avoid contamination from the nearby Langmuir wave. The three dotted lines in each panel represent exponential fittings to energy profiles.

particle resonant coupling ($\omega - n\Omega_{ce} - k_z v_z = 0$, where n is the harmonic number).

Second is the decrease of growth rates of the three linearly excited modes (UH, Z, and W) with increasing v_e. See Figure 3 for lines fitting the linear stage of the mode growth. For $v_e = 0.15c$ the growth rates of UH, Z, and W modes are 0.34, 0.32, 0.23 $\Omega_{ce} n_e/n_0$, and for $v_e = 0.3c$ the rates are 0.22, 0.17, 0.28 $\Omega_{ce} n_e/n_0$ (see Ni et al. 2020), respectively. For $v_e = 0.4c$ the growth rates are similar to those of $v_e = 0.3c$. This variation of growth rate directly affects the duration of the linear stage and the maximum intensity of the mode. In general, the duration of linear stage of UH mode becomes larger with increasing v_e, being $\sim 1000\,\omega_{pe}^{-1}$ for $v_e = 0.15c$ and $\sim 1500\,\omega_{pe}^{-1}$ for both $v_e = 0.3c$ and $v_e = 0.4c$. The duration of the Z mode linear growth also presents a similar increasing trend with increasing v_e. For the W mode, the duration of the linear stage decreases as v_e increases from $0.15c$ to 0.3–$0.4c$.

Last is the change of directional pattern of the H emission. The results presented here confirm the basic picture first described by Ni et al. (2020) that escaping radiations can be excited by energetic electrons with the DGH distribution. The obtained emission, in particular, the H emission, exhibits quite different characteristics with increasing v_e. For $v_e = 0.15c$ H radiates mainly along the quasi-perpendicular to perpendicular direction, while for larger v_e H exhibits a very-different quadrupolar-like pattern. This difference is likely due to the change of its mother wave, i.e., the UH mode, whose coalescence results in the generation of the H mode according to Ni et al. (2020). As mentioned, for $v_e = 0.15c$ the UH mode has a quite-limited range in both propagating angles (θ_{kB}) and value of k; this affects the emission pattern of H through the matching condition of wavenumber. On the other hand, for large v_e the UH mode distributes wider in the $\boldsymbol{k}$ space, this makes the coalescence of the UH mode close to those reported for the isotropic Langmuir waves (see, e.g., Ziebell et al. 2015) and results in the quadrupolar-like pattern of radiation.

In addition, the intensity of plasma radiations (H or O-F) are comparable for the three cases, despite the significant change of directional pattern of the H mode. The H mode is significantly stronger than the O-F mode ($\theta_{kB} > 15°$) by about 2–3 orders of magnitude, while the O-F mode is only marginally stronger than the background noise. The H emission concentrates around frequency of $\sim 19.4\,\Omega_{ce}$ for $v_e = 0.15c$ and $\sim 19.0\,\Omega_{ce}$ for $v_e = 0.4c$.

3.2. The DPR Effect

To simulate the DPR effect, we vary ω_{pe}/Ω_{ce} within two harmonic bands (9.5–11.5) with a fixed value of v_e(=0.15c). This allows us to observe two complete periods of the DPR effect, which leads to high and low values of growth rates and wave intensities. The basic underlying assumption is that the spatial-temporal scales of variation of ω_{pe}/Ω_{ce} should be much larger than corresponding scales of wave excitation. This allows us to use PIC simulations within homogeneous background (using different ω_{pe}/Ω_{ce}) to simulate the DPR effect that rises only in a nonuniform media.

Figure 4 presents the wave intensity map in the $\boldsymbol{k}$ space, and Figure 5 presents the ω–k dispersion analysis. From left to right, results with various ω_{pe}/Ω_{ce} in the range of [9.5, 11.5] are presented. As seen from the dispersion analysis shown in Figure 4(a), varying ω_{pe}/Ω_{ce} mainly affects the distribution (in $\boldsymbol{k}$ space) of the UH mode with large intensity. Such distribution also oscillates with varying ω_{pe}/Ω_{ce} as clearly seen from the figure. For example, when ω_{pe}/Ω_{ce} is close or equal to 10 or 11, the range of k is constrained to very-narrow ranges along the perpendicular to quasi-perpendicular direction, consistent with the ω–k diagram (see Figure 5(a)). For the Z mode, when $\omega_{pe}/\Omega_{ce} = 10$ or 11, no wave exists for small k along the perpendicular direction (Figure 5(b)), while for $\omega_{pe}/\Omega_{ce} = 10.25$ and 11.25 the mode mainly distributes around a region of small k. For other noninteger values of ω_{pe}/Ω_{ce}, it distributes over a wider region of k. Its frequency increases with increasing ω_{pe}/Ω_{ce}, as expected. The ranges of ω and k of the parallel propagating W mode do not change considerably with ω_{pe}/Ω_{ce} according to Figure 5(d), due to its nature of excitation (i.e., the $n = 1$ cyclotron resonance).

The temporal profiles of wave energy have been plotted in the upper panels of Figure 6, the linear growth rates obtained by exponential fittings have been plotted in panel (d), mode

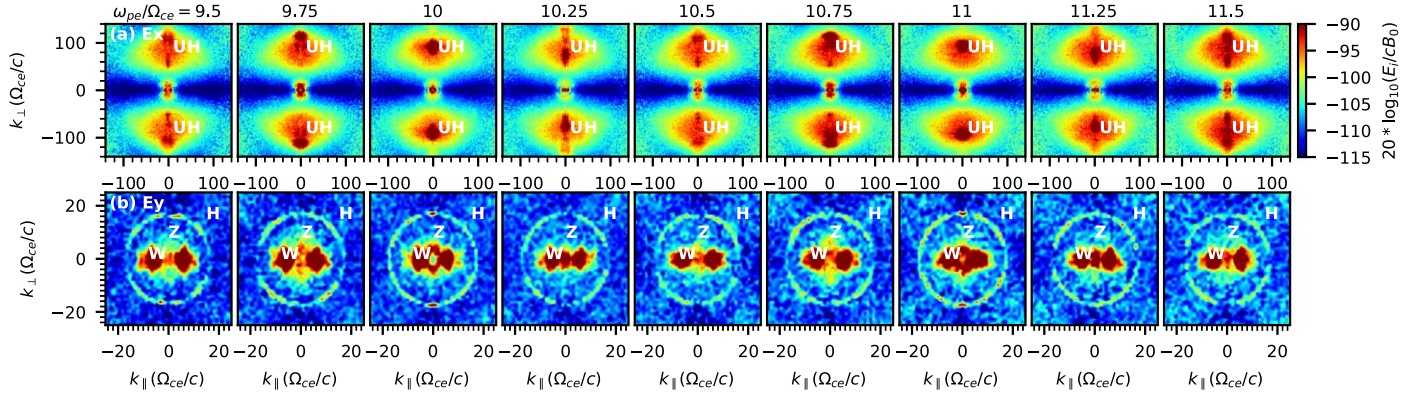

Figure 4. The wave intensity map in ($k_\parallel$, $k_\perp$) space with $\omega_{pe}/\Omega_{ce} = 9.5$–11.5 over the interval of $1500 < \omega_{pe}t < 2500$. Lower panels are zoom-in versions of upper panels.

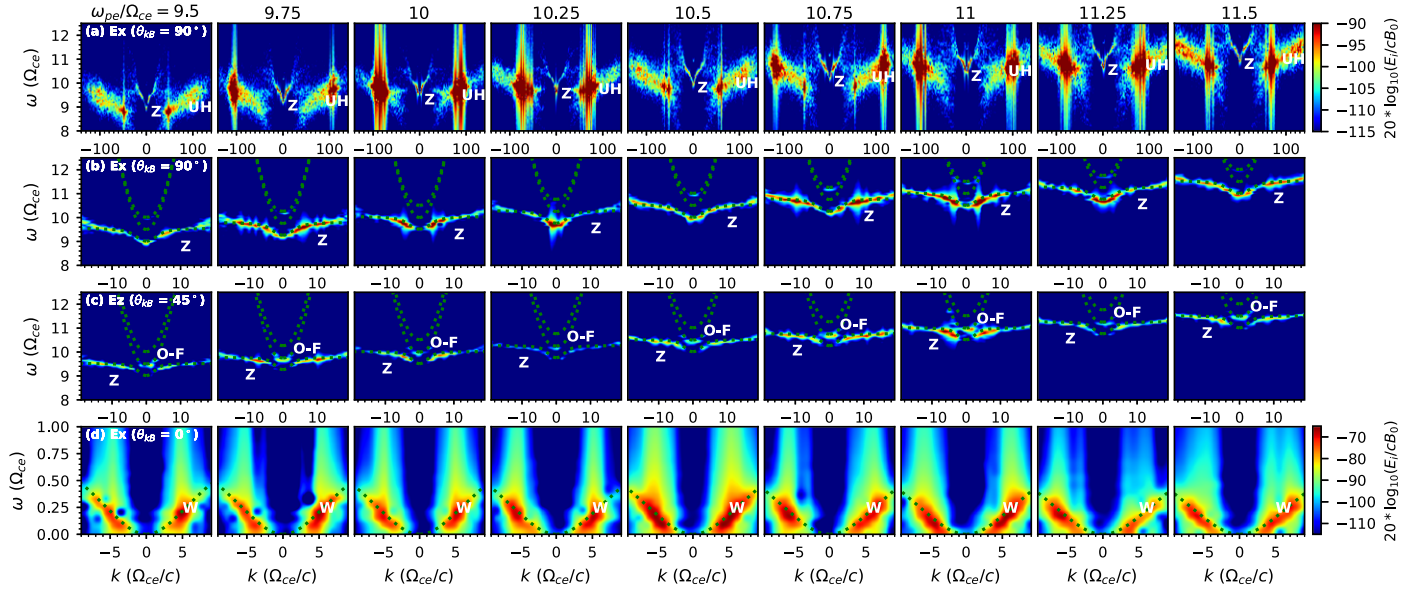

Figure 5. The ω–k dispersion curves for different modes over times $2500 < \omega_{pe}t < 3500$ along the directions labeled on the corresponding panels. Each column represents result for one specific value of ω_{pe}/Ω_{ce}. The green dotted lines represent the dispersion curves of four modes (X, O, Z, and W) of the theoretical magneto-ionic theory. Panels (a)–(c) use the same colorbar (next to panel (a)), and panel (d) uses the colorbar next to it.

energies at the end of the simulations have been plotted in the last two panels (e)–(f). In all cases, the UH mode experiences significant damping after its saturation stage, we therefore also plotted the maximum energy of UH mode in Figure 6(e). For other modes, no significant damping is observed.

Consistent with the results presented above, the UH mode dominates the growth of waves during the first 1000 ω_{pe}^{-1}, reaching the maximum energy level around or slightly higher than $10^{-4}\,E_{k0}$ and then damping to an energy level around $10^{-5}\,E_{k0}$. During the saturation and damping stages of the UH mode, the W mode becomes the dominant one reaching an energy level around $10^{-3}\,E_{k0}$. The Z mode only reaches a weak level of 10^{-8}–$10^{-7}\,E_{k0}$.

The DPR effect can be clearly seen from the periodic variation of both growth rate and energy of UH and Z modes (see lower panels of Figure 6). The growth rates manifest variations of two complete periods, reaching the minima at $\omega_{pe}/\Omega_{ce} = 9.75$ and 10.75 and the maxima at $\omega_{pe}/\Omega_{ce} = 10.25$ and 11.25. The period of variation is Ω_{ce} as expected, yet the peaks do not lie exactly at the integer times of Ω_{ce}, this is due to the thermal effect and the deviation from perpendicular propagation of the two modes, as already found earlier by theoretical analysis (see, e.g., Winglee & Dulk 1986; Yasnov & Karlický 2004; Benáček et al. 2017; Li et al. 2019). The ratio of the maximum to minimum growth rates achieved, respectively, at $\omega_{pe}/\Omega_{ce} = 10.25$ and 10.75 is ∼2.6 for the UH mode and ∼2.8 for the Z mode. The growth rate of the W mode does not present a similar double-period DPR pattern, which is mainly associated with the fundamental gyroresonance ($n = 1$), while the DPR effect is mainly carried by modes (UH and Z) that are excited at a large number of harmonics.

The maximum energy of the UH mode (indicated as $\mathrm{UH_{max}}$ in Figure 6(e)) also presents a similar double-period variation, a direct imprint of the DPR effect. A similar trend is observed from the profile of the Z mode energy at the end of simulations (Figure 6(f)). Yet the energy of the UH mode at the end of simulations presents almost-opposite trend of variation, it reaches the minimum level at $\omega_{pe}/\Omega_{ce} = 10.25$ and maximum around $\omega_{pe}/\Omega_{ce} = 10.0$ and 10.75. The energy of the W mode at the end of simulations first decreases and then increases with increasing ω_{pe}/Ω_{ce}, quite different from the variation of UH and Z modes. This means that variation of ω_{pe}/Ω_{ce} does affect the growth of the W mode, yet not in accordance with the DPR effect. This is also likely due to the point that the W mode is

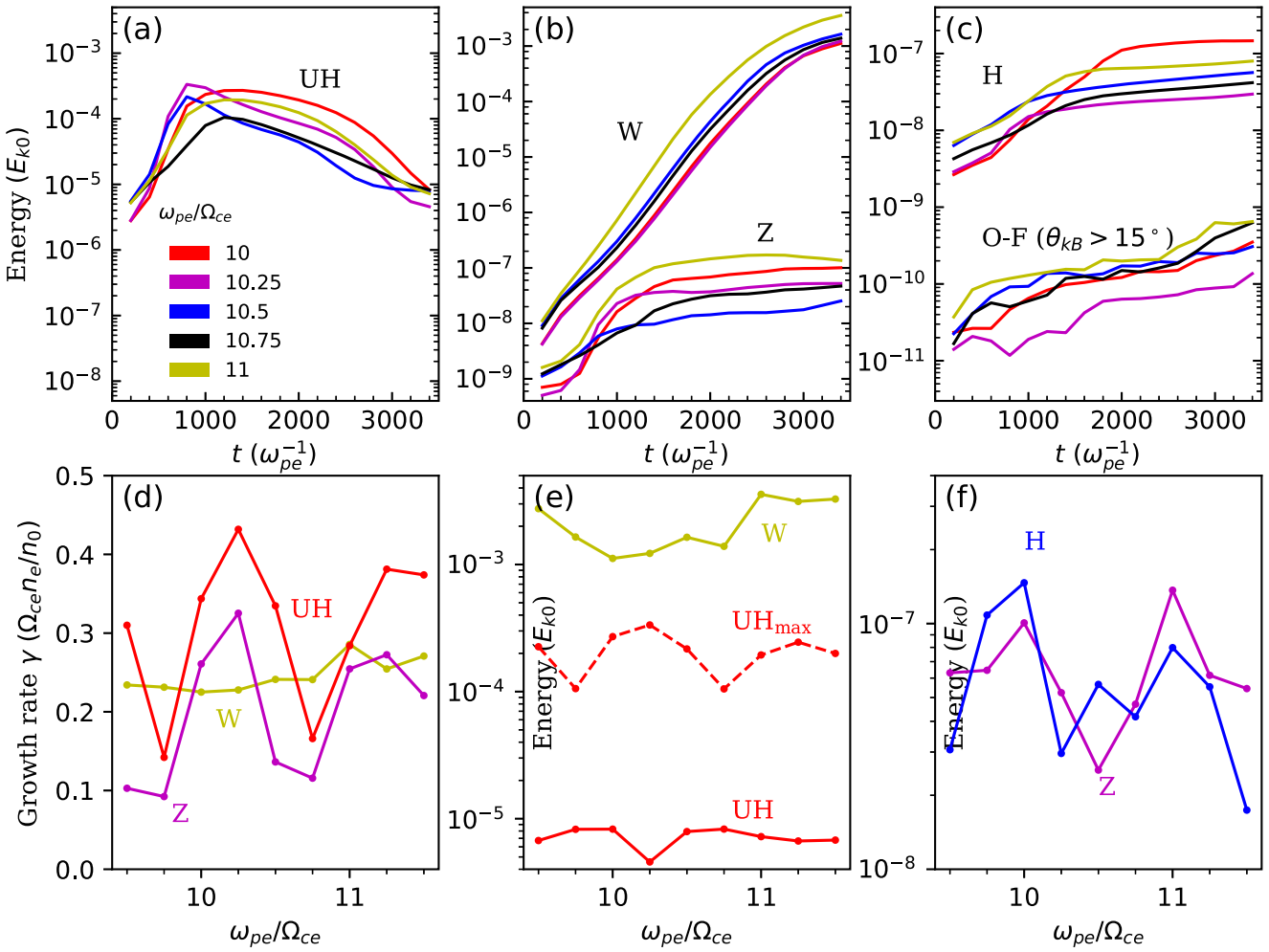

Figure 6. (a)–(c) The temporal energy profiles of the five modes with $v_e = 0.15c$ and $\omega_{pe}/\Omega_{ce} = 10$, 10.25, 10.5, 10.75, 11, normalized to E_{k0}. (d) The fitted linear growth rate of UH, Z, and W modes. (e)–(f) The variation of final energy of different modes with ω_{pe}/Ω_{ce}, the red dashed line represents the maximum energy profile of the UH mode.

associated with the $n = 1$ gyroresonance. Note that the W mode has not reached its full saturation level at the end of simulations.

3.3. The ECMI-induced Plasma Emission with ZPs

According to the PIC simulation and further analysis presented in Ni et al. (2020), plasma emission of both F (O mode) and H bands can be generated through nonlinear coalescence of waves that are excited by energetic electrons of the DGH distribution. The H emission is generated through coalescence of almost-counter-propagating UH modes and the F emission is generated through coalescence of almost-counter-propagating Z and W modes. Thus, it is intriguing to further examine how the DPR effect affects properties of the obtained plasma emission.

From Figure 6(c), the H emission is stronger than the O-F emission by about 2 orders of magnitude. Further inclusion of the energy of quasi-parallel propagating O-F mode does not affect this result. The final energy of H emission varies within a range of 10^{-8}–$10^{-7}\,E_{k0}$, at the same level of the energy of the Z mode; while the O-F mode is only slightly stronger than the background noise as mentioned, within a range of 10^{-10}–$10^{-9}\,E_{k0}$. For the H emission, the energy exhibits periodic variation, reaching the local maxima at $\omega_{pe}/\Omega_{ce} = 10$ and 11 and the local minima at $\omega_{pe}/\Omega_{ce} = 9.5$, 10.25, and 11.5, for the parameters considered here. This gives rise to the well-known ZP feature of solar radio bursts. The obtained peak-valley ratio of the H intensity is about 4, consistent with the observed range of intensity contrast of solar ZPs (see, e.g., Chen et al. 2011; Chernov et al. 2012, and Tan et al. 2014b). Note that the variation profile of the H intensity is basically opposite to that of the growth rate and the maximum energy of the UH mode, yet in line with its final energy profile (see Figure 6(e)).

For the O-F mode, evaluation of energy may suffer from certain error if considering the contamination from nearby Z mode wave and its weak intensity. Thus, we do not further analyze the energy variation of the O-F mode with ω_{pe}/Ω_{ce}. In reality the weak signals of the O-F mode can be easily buried by the strong H emission and thus may not be observable.

From the $\boldsymbol{k}$-space dispersion diagram (Figure 4(b)), the H emission exhibits certain variation in directional pattern with ω_{pe}/Ω_{ce}. When $\omega_{pe}/\Omega_{ce} = 10$ and 11, the intensity of the H emission peaks along the perpendicular direction. This is similar to what we have presented in Section 3.1, likely due to the mentioned specific concentration of the UH mode in the $\boldsymbol{k}$ space. For noninteger values, the H emission exhibits somewhat complex patterns of radiation, it may get enhanced at different propagation angles, and may get weakened along the

perpendicular direction (e.g., for cases with $\omega_{pe}/\Omega_{ce} = 9.75$, 10.25, and 11.5). The corresponding distribution of UH modes (see Figure 4(a)) is far from isotropic, thus the theory of coalescence of Langmuir waves with isotropic distribution, which leads to a quadrupolar pattern of radiation does not apply here.

4. Summary and Discussion

ZPs are intriguing features observed in the dynamic spectra of solar radio bursts. It carries valuable information of plasmas and magnetic field in the corona and has been used for diagnostic purpose. The DPR effect in plasmas with large ω_{pe}/Ω_{ce} represents the most-accepted scenario for ZPs. Yet earlier studies were mostly based on linear theoretical analysis of electrostatic waves such as the UH mode. This study presents the first PIC study simulating DPR and ZPs simultaneously on the basis of the ECMI-driven plasma emission process.

According to our simulations, both electrostatic UH wave and electromagnetic Z and W modes are excited through ECMI driven by energetic electrons of DGH distribution. Properties of both UH and Z modes are consistent with the DPR effect. The induced plasma emissions at H and F bands are obtained through nonlinear wave–wave interaction, consistent with our earlier study (Ni et al. 2020). The H emission dominates over the F emission in intensity by about 2 orders in magnitude, this indicates that the ZPs arise from the H emission, rather than the F emission as assumed in many studies (e.g., Zlotnik et al. 2014; Chernov 2015; Kaneda et al. 2017). The peak-valley contrast of intensity of the H emission is found to be ~4, consistent with some observational reports. These results are critical to the understanding of solar ZPs and further diagnostic efforts using radio data.

In addition, we found that the energy (or velocity) of energetic electrons (represented with v_e) is important to the characteristics of the UH mode and the radiation pattern of the H emission. For smaller $v_e(=0.15c)$, the UH mode concentrates within a quite-limited range in the $\boldsymbol{k}$ space (mainly along the perpendicular-to-quasi-perpendicular direction), for larger $v_e(=0.3c$ and $0.4c)$ the UH mode distributes more diffusively over a wider range; the H emission for $v_e(=0.15c)$ achieves the maximum intensity along the perpendicular direction while for larger v_e it presents a quadrupolar-like radiation pattern lack of perpendicular propagation. This result is obtained for a fixed value of $\omega_{pe}/\Omega_{ce}(=10)$. Note that varying ω_{pe}/Ω_{ce} also affects the distribution and radiation pattern of various wave modes.

In the present study, the DPR effect and the induced plasma emission of ZPs are investigated with various ω_{pe}/Ω_{ce} and fixed $v_e(=0.15c)$. In future, PIC simulations with larger v_e shall be conducted to further explore its effect. In addition, the DPR effect is simulated here with independent PIC simulations for different values of ω_{pe}/Ω_{ce}, assuming the spatial-temporal scales of inhomogeneity are much larger than the scales of wave excitation. Studies within a larger domain incorporating inhomogeneous distribution of magnetic field strength and plasma density should be carried out so as to simulate the DPR effect and generation of ZPs self-consistently.

This study is supported by the National Natural Science Foundation of China (11790303 (11790300), 11973031, 11750110424, and 11873036). The authors acknowledge the Beijing Super Cloud Computing Center (BSCC, URL: http://www.blsc.cn/) for providing high-performance computing (HPC) resources, and the open-source Vector-PIC (VPIC) code provided by Los Alamos National Labs (LANL). The authors acknowledge the helpful discussions with Dr. Xiaocan Li (LANL) and Prof. Quanming Lu (USTC, University of Science and Technology of China). The authors are grateful to the anonymous referee for valuable comments.

Table 1
Setup Parameters of Various Cases for the Convergence Test

Case	NPPC	n_x	n_z	dx (λ_D)	dz (λ_D)
Ref.	1000	1024	1024	3.25	3.25
A	1000	1024	1024	3.25	3.25
B	1000	2048	2048	3.25	3.25
C	250	2048	2048	3.25/2	3.25/2
D	200	1024	1024	3.25	3.25
E	500	1024	1024	3.25	3.25
F	2000	1024	1024	3.25	3.25
G	4000	1024	1024	3.25	3.25

Note. NPPC is the number of macro-particles per species per cell, n_x and n_z are numbers of grid cells, dx and dz are the cell sizes, and λ_D is the Debye length of the background electrons. The reference case is taken to be the case presented in Section 3.2 with $\omega_{pe}/\Omega_{ce} = 10$, $v_e = 0.15c$, and NPPC = 1000. Parameters not listed are set to be the same as those of the reference case.

Appendix
Convergence Test of the PIC Simulation

The convergence test of PIC simulations is computationally expensive. Here we limit the test to verify the significance of escaping radiation and intensity variations of various wave modes with time. Setups of these test cases are summarized in Table 1.

Note that the number of grid points, NPPC (number of particles per cell), computational domains, and durations of the present study are either much higher than those earlier studies or comparable to those latest studies. For example, Kasaba et al. (2001) used 16 particles per cell for background particles and 4 for the electron beam, while in Umeda (2010) the NPPC is set to be 256, in Thurgood & Tsiklauri (2015) the NPPC is set to be 1000, and it is set to be 2000 in Zhou et al. (2020).

Similar convergence test has been done earlier by Ni et al. (2020), here we present a more-complete test in accordance with the parameters adopted here. These cases are briefly explained below, in comparison to the reference case, which is taken to be the case presented in Section 3.2 with $\omega_{pe}/\Omega_{ce} = 10$, $v_e = 0.15c$, and NPPC = 1000.

1. Case A: for all particles with the Maxwellian distributions, no energetic particles are involved, to check the level of the organized thermal noise.
2. Case B: with a larger number of spatial grid points and thus a larger domain, to check the effect of grid number and size of the domain.
3. Case C: with less NPPC yet the same total number of particles in the same spatial domain, with smaller cell size yet more grid points, to check the effect of NPPC and size of cells.
4. Cases D–G: with various NPPC from 200 to 4000, to check the effect of NPPC.

Comparisons of these cases with the reference case are presented in Figures 7 and 8, where energy profiles of

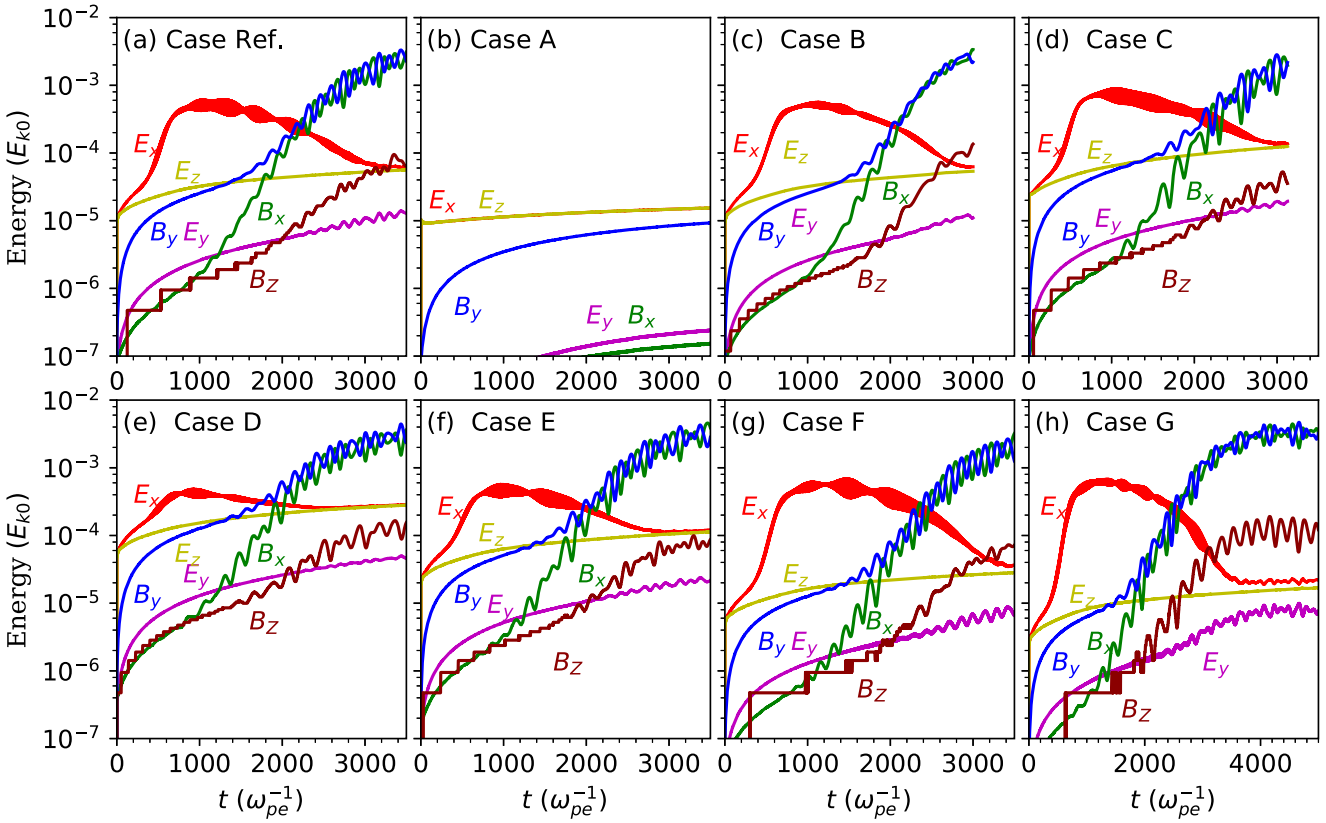

Figure 7. Temporal profiles of energies of various field components (E_x, E_y, E_z, B_x, B_y, and B_z) normalized to the initial kinetic energy of the DGH electrons (E_{k0}). See Table 1 for the setup parameters of each case.

electromagnetic field components and those of various wave modes are plotted. We reach the following conclusions:

1. Resolving capability of the simulations:
   According to the setup of the reference case, the frequency and wavenumber ranges that can be resolved are [0, 32] Ω_{ce} and [−536, 536] Ω_{ce}/c, respectively. The corresponding resolutions of the DFT analysis are 0.06 Ω_{ce} for the frequency (ω) (for the time interval of 1000 ω_{pe}^{-1}) and 1.04 Ω_{ce}/c for the wavenumber (k). The setup seems to be sufficient to properly resolve most modes except the O-F mode, which is characterized by a range of relatively small wavenumber [0, 3] Ω_{ce}/c. Thus, in the convergence test we paid special attention to the significance and variation of the O-F mode.
2. Magnitudes and variation profiles of intensities:
   Intensities of all field components and relevant wave modes reach levels that are significantly higher than those in the Maxwellian case (A), even the O-F mode, the weakest one, is about one-order of magnitude higher than the level of the corresponding thermal noise.
3. Effect of NPPC and other factors:
   As long as the NPPC is greater than 500, intensities of field components and wave modes (except the O-F mode) do not vary considerably with the domain size and cell size. With increasing NPPC, it takes more time for the O-F mode to rise toward the asymptotic intensity. To show its rising trend in Case G with NPPC = 4000, we extend the simulation time to 5000 ω_{pe}^{-1}. Note that the O-F mode reaches similar intensities at the end of each simulation.

Furthermore, to verify the validity of the underlying emission mechanism, especially, the generation of the O-F mode emission from the coalescence of Z and W modes, we conducted another study with the wave-pumping technique. The result is also obtained with the VPIC code. The dispersion analyses for three cases are examined, including the case (Z) in which only the Z mode has been pumped into the system, the case (W) in which only the W mode has been pumped, and the case (Z+W) in which both modes have been pumped. The results confirm robustly the generation of the O-F mode emission through the proposed ECMI-induced plasma emission process. The wave-pumping study will be published elsewhere and not shown here (Ni et al. 2021, submitted to Physics of Plasmas).

The above convergence test and additional study indicate that for wave modes except for the O-F mode the quantitative results presented in the manuscript are convincing, while for the O-F mode the quantitative intensity evaluations may suffer from large uncertainties due to the limited resolving capability of its wavenumber, as well as the contamination from the spectrally nearby Z mode. Thus, in the study we did not present the variation profiles of the O-mode intensity with ω_{pe}/Ω_{ce}.

ORCID iDs

Chuanyang Li https://orcid.org/0000-0001-9707-584X
Yao Chen https://orcid.org/0000-0001-6449-8838
Baolin Tan https://orcid.org/0000-0003-2047-9664
Hao Ning https://orcid.org/0000-0001-8132-5357

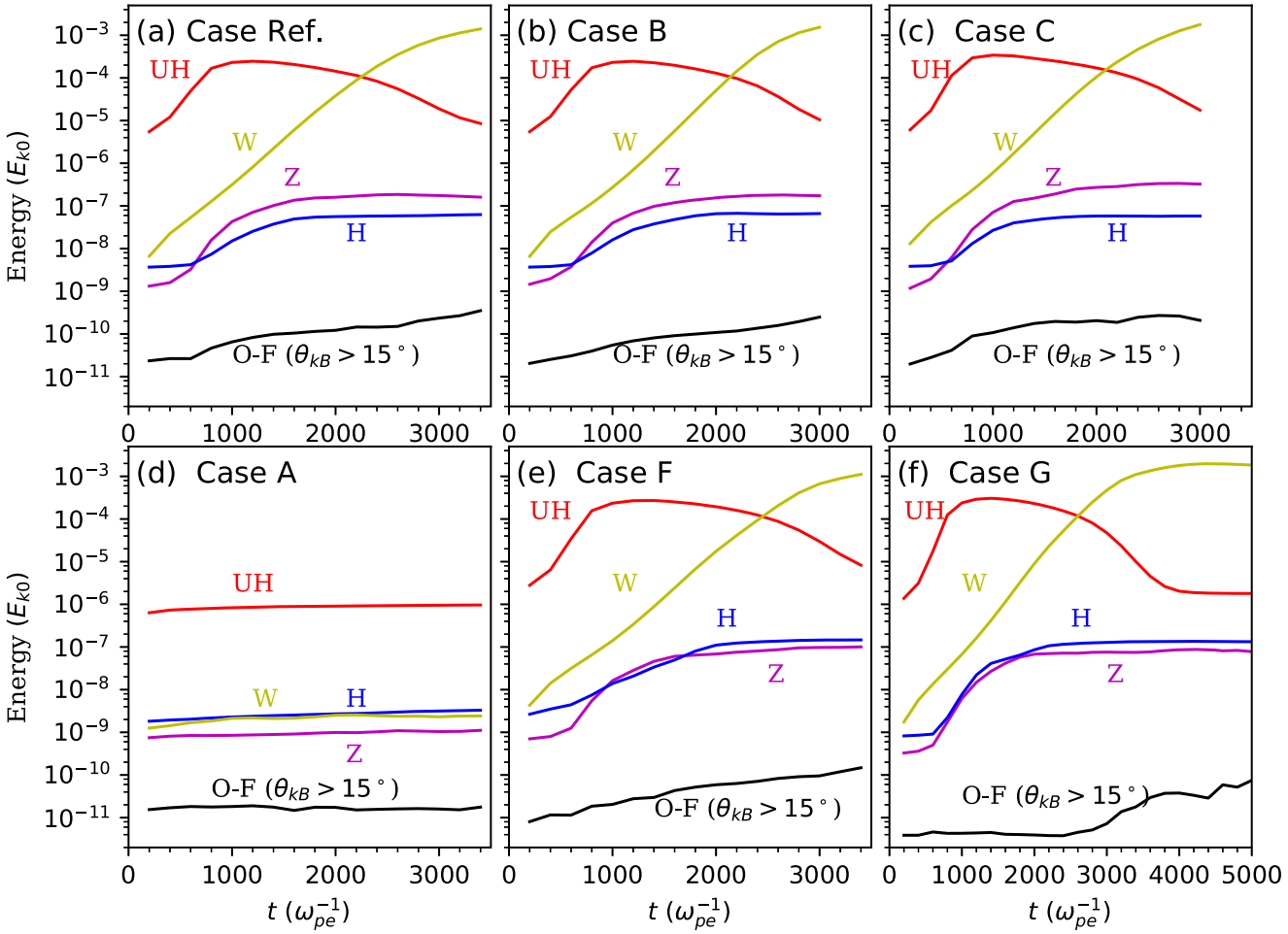

Figure 8. The temporal energy profiles of UH, Z, W, H, and O-F modes of different cases listed in Table 1.

References

Benáček, J., & Karlický, M. 2018, A&A, 611, A60
Benáček, J., & Karlický, M. 2019, ApJ, 881, 21
Benáček, J., Karlický, M., & Yasnov, L. V. 2017, A&A, 598, A106
Benz, A. 2002, in Plasma Astrophysics, Kinetic Processes in Solar and Stellar Coronae, Astrophysics and Space Science Library, Vol. 279, ed. A. Benz (Dordrecht: Kluwer)
Bowers, K. J., Albright, B. J., Bergen, B., et al. 2008a, Proc. IEEE, SC 08, 63
Bowers, K. J., Albright, B. J., Yin, L., et al. 2008b, PhPl, 15, 055703
Bowers, K. J., Albright, B. J., Yin, L., et al. 2009, JPhCS, 180, 012055
Chen, B., Bastian, T. S., Gary, D. E., & Jing, J. 2011, ApJ, 736, 64
Chernov, G. (ed.) 2011, Fine Structure of Solar Radio Bursts (Berlin: Springer)
Chernov, G. 2015, arXiv:1512.06311
Chernov, G. P. 1990, SoPh, 130, 75
Chernov, G. P., Sych, R. A., Meshalkina, N. S., et al. 2012, A&A, 538, A53
Dory, R. A., Guest, G. E., & Harris, E. G. 1965, PhRvL, 14, 131
Ginzburg, V. L., & Zhelezniakov, V. V. 1958, SvA, 2, 653
Kaneda, K., Misawa, H., Iwai, K., et al. 2017, ApJ, 842, 45
Karlický, M. 2013, A&A, 552, A90
Kasaba, Y., Matsumoto, H., & Omura, Y. 2001, JGR, 106, 18693
Kuijpers, J. 1975a, SoPh, 44, 173
Kuijpers, J. 1975b, A&A, 40, 405
Kuznetsov, A. A. 2005, A&A, 438, 341
LaBelle, J., Treumann, R. A., Yoon, P. H., et al. 2003, ApJ, 593, 1195
Ledenev, V. G., Yan, Y., & Fu, Q. 2006, SoPh, 233, 129
Li, C., Chen, Y., Kong, X., et al. 2019, ApJ, 880, 31
Ni, S., Chen, Y., Li, C., et al. 2020, ApJL, 891, L25
Ni, S., Chen, Y., Li, C., et al. 2021, PhPl, submitted
Slottje, C. 1972, SoPh, 25, 210
Smerd, S. F., & Dulk, G. A. 1971, in IAU Symp. 43, Solar Magnetic Fields, ed. R. Howard (Dordrecht: Reidel), 616
Stewart, R. T. 1985, Solar Radiophysics: Studies of Emission from the Sun at Metre Wavelengths (Cambridge: Cambridge Univ. Press), 361
Tan, B. 2010, Ap&SS, 325, 251
Tan, B., Tan, C., Zhang, Y., et al. 2014a, ApJ, 780, 129
Tan, B., Tan, C., Zhang, Y., et al. 2014b, ApJ, 790, 151
Thurgood, J. O., & Tsiklauri, D. 2015, A&A, 584, A83
Umeda, T. 2010, JGRA, 115, A01204
Vasanth, V., Chen, Y., Feng, S., et al. 2016, ApJL, 830, L2
Vasanth, V., Chen, Y., Lv, M., et al. 2019, ApJ, 870, 30
Vlahos, L., Gergely, T. E., & Papadopoulos, K. 1982, ApJ, 258, 812
Wild, J. P., & Smerd, S. F. 1972, ARA&A, 10, 159
Winglee, R. M., & Dulk, G. A. 1986, ApJ, 307, 808
Wu, C. S., & Lee, L. C. 1979, ApJ, 230, 621
Yasnov, L. V., & Karlický, M. 2004, SoPh, 219, 289
Zheleznyakov, V. V., & Zlotnik, E. Y. 1975, SoPh, 44, 461
Zheleznyakov, V. V., Zlotnik, E. Y., Zaitsev, V. V., et al. 2016, PhyU, 59, 997
Zhou, X., Muñoz, P. A., Büchner, J., et al. 2020, ApJ, 891, 92
Ziebell, L. F., Yoon, P. H., Petruzzellis, L. T., et al. 2015, ApJ, 806, 237
Zlotnik, E. Y. 2013, SoPh, 284, 579
Zlotnik, E. Y., Zaitsev, V. V., & Altyntsev, A. T. 2014, SoPh, 289, 233